EES Batteries

PAPER

View Article Online
View Journal

Cite this: DOI: 10.1039/d6eb00021e

Nickel-dependent interfacial chemistry in layered oxide cathodes: insights from X-ray photoelectron spectroscopy and electrochemical quartz crystal microbalance measurements

Monica J. Theibault, [a] Dennis Nordlund,[b] Marca Doeff *[a] and Wei Tong *[a]

NMC ($LiNi_xCo_yMn_zO_2$; $x + y + z \approx 1$) cathodes are widely used in Li-ion batteries for long-range vehicle applications. The Ni content in NMC cathodes directly affects practical capacity and, therefore, the energy densities of Li-ion batteries. Ni-rich NMC cathodes, however, suffer a tradeoff between increased energy density and decreased cycle life. In this study, we investigate the tradeoff between capacity and cycle life by thoroughly characterizing the interfacial chemistry of two NMC materials, $LiNi_{0.6}Co_{0.2}Mn_{0.2}O_2$ (NMC622) and $LiNi_{0.9}Co_{0.05}Mn_{0.05}O_2$ (NMC9055), in an attempt to understand the impact of Ni content on surface properties and cell performance. *In situ* electrochemical quartz crystal microbalance (EQCM) measurements were employed on NMC622 and NMC9055 along with $LiNi_{0.8}Co_{0.1}Mn_{0.1}O_2$ (NMC811) as an additional benchmark. Combined with X-ray photoelectron spectroscopy (XPS) and X-ray absorption spectroscopy (XAS), we detected the severe interference of side reactions with lithium re-insertion on NMC9055 discharge compared to NMC622. These experiments indicate that, for lower nickel content NMC622, these reactions are largely constrained to the very surface and reversible in nature, while, for higher nickel content NMC9055, parasitic reactions penetrate deeper into the bulk and contribute to capacity fade.

Received 26th January 2026,
Accepted 21st March 2026

DOI: 10.1039/d6eb00021e

rsc.li/EESBatteries

Broader context

Increasing Ni-content in NMC cathodes ($LiNi_xMn_yCo_zO_2$ ($x + y + z \cong 1$)) results in higher practical capacities but comes at the expense of cycle life. In this work, surface-sensitive X-ray and *in situ* electrochemical quartz crystal microbalance (EQCM) techniques were used to study the effect of increased Ni content on electrochemical behavior and characterize cathode–electrolyte interfacial reactions. The EQCM experiments show that Li^+ insertion into NMC9055 is accompanied by deposition of decomposition products on cathode surfaces. NMC9055 cathodes exhibit significantly more pronounced chemical reactions that lead to dissolution or deposition of surface species during electrochemical cycling compared to NMC622 and NMC811, suggesting that the surfaces are more reactive. In NMC622, side reactions are mainly confined to near surface regions, whereas in NMC9055, parasitic reactions penetrate deeper into the bulk and contribute to the capacity fade.

Introduction

Expansion of Li-ion batteries beyond their current limitations, such as for long-range applications in electrical transportation, requires development of advanced cathode materials with higher energy density.[1–3] Ni-rich layered oxides, $LiNi_xMn_yCo_zO_2$ (NMC, $x + y + z \approx 1$, where $x > 0.6$), are capable of achieving higher practical capacities, greater energy densities, and lower cost; the practical capacity increase scales approximately with the proportion of Ni within the cathode.[4,5] However, this comes with a concomitant decrease in cycle life, particularly when cycling to higher voltages.[6–8]

Access to greater Li^+ extraction and therefore higher practical capacities, without the resultant negative effects on capacity retention, is necessary for the further advancements of Li-ion batteries, to allow for longer distances travelled on a single charge. Past investigations of numerous NMCs, with Ni content of 0.6 or higher, have explored the impact of cathode microcracking during cycling,[9,10] NMC surface reconstruction,[1,5,11] and formation of metal–organic surface films that form ionic barriers at the cathode–electrolyte interface (CEI).[12,13] Two aspects of this discussion that remain relatively understudied, however, are rigorous comparisons among Ni-rich NMCs with different Ni contents, especially, a systematic study of surface layers that form during cycling for each

[a]*Energy Technologies and Systems Division, Lawrence Berkeley National Laboratory, Berkeley, CA 94720, USA. E-mail: weitong@lbl.gov, mmdoeff@lbl.gov*
[b]*Stanford Synchrotron Radiation Lightsource, SLAC National Accelerator Laboratory, Menlo Park, CA 94025, USA*

material. A key question of Ni-rich NMC chemistry is: what is the tradeoff between nickel content and charge voltage in terms of overall electrochemical performance, such as initial capacity, coulombic efficiency, and long-term cycling stability? To this purpose, two Ni-rich cathodes, $LiNi_{0.6}Mn_{0.2}Co_{0.2}O_2$ (NMC622) and $LiNi_{0.9}Mn_{0.05}Co_{0.05}O_2$ (NMC9055), were chosen to compare their electrochemistry and surface properties. One goal was to determine the potential limits at which the capacity of NMC9055 is similar to that of NMC622. Additionally, what are the side reactions occurring on NMC cathodes when they have different Ni content and are charged to different potentials, and how do they contribute to this tradeoff?

In general, the surface chemistry, including the cathode–electrolyte interface (CEI), of NMCs is complex and its close comparison against Ni content remains relatively understudied compared to the bulk properties. Depth-dependent surface characterization of Ni-rich NMCs have primarily focused on Ni oxidation states and omit the link with depth-dependent CEI formation. The CEI forms specifically at higher potentials,[14,15] and is a very thin (<1 nm) surface film formed from decomposition products during charging and discharging. Unlike the solid electrolyte interphase (SEI) at anode surfaces, the CEI, once formed, does not typically passivate the cathode surface. The CEI is particularly important for Ni-rich NMCs, as they are prone to microcracking, which results in penetration of the electrolyte and therefore formation of fresh CEI (concomitant with consumption of electrolyte) deeper into the bulk cathode.[5,13] Thus, studies of the CEI must contend with its variations at different depths, posing additional challenges. There has been success in state of the art modeling techniques towards understanding of CEI formation, evolution, and Li transport.[16] However, successful implementation of models towards filling in knowledge gaps related to depth-dependent CEI formation requires a positive feedback loop alongside rigorous, generalizable experimental studies of depth-dependent CEI formation.

In this study, the electrochemistry of NMC622 and NMC9055 was compared, in an attempt to find a "sweet spot" of capacity *versus* potential range. Ultimately, however, it was determined that the instability of NMC9055 does not solely depend on the charging potential. Then, charged cathodes of NMC622 and NMC9055 were thoroughly analyzed by surface-sensitive soft X-ray absorption spectroscopy (XAS) and X-ray photoelectron spectroscopy (XPS) in order to determine the depth-dependent chemical components of surface compounds, their evolution during cycling, as well as impact on electrochemical instability. Finally, the electrochemical quartz microbalance (EQCM) technique was applied to a series of NMCs (NMC622, NMC811, and NMC9055) to provide additional insights into the surface chemistry under extended cycling.

Experimental methods

Cell assembly

Commercially available NMC9055 (MSE Supplies) and NMC622 (Targray) were used for this study without further treatment. Each active material was mixed with acetylene black and polyvinylidene fluoride (PVDF) in a ratio of 8 : 1 : 1 (wt.%), with *N*-methylpyrrolidone (NMP), in a Thinky mixer for 5 minutes at 2000 rpm. The total dry powder mass was ~2 g before addition of NMP. The slurry was then sonicated for 10 minutes before being mixed in a Thinky mixer for another 5 minutes at 2000 rpm. The mixture was then cast onto a carbon coated aluminum current collector to form the cathode and dried in a vacuum oven for 12 hours at 120 °C. Coin cells were assembled with a $\frac{1}{2}$ inch diameter cathode (approximate mass loadings of 6.0–6.5 mg cm^{-2}), a 1 mm thick Whatman GF/F separator, a 5/8-inch diameter lithium metal anode, and 120 μL of an electrolytic solution of $LiPF_6$ in 1 : 1 ethylene carbonate/diethyl carbonate (EC/DEC).

Cell testing

Electrochemical cycling was performed on a Biologic VMP-3 multichannel cycler.

Constant current (CC) charging. NMC622 half-cell rate tests (1C = 180 mAh g^{-1}) were performed between 2.8 V and various charge cutoff voltages (4.3 V, 4.4 V, 4.5 V, and 4.7 V) for initial five cycles at 0.1C with four successive cycles at each of the following rates: 0.2C, C/3, 0.5C, 1C, 0.5C, C/3, and back to 0.1C. NMC9055 half-cell rate tests (1C = 200 mAh g^{-1}) were performed between 2.8 V and charge cutoffs of 4.2 V, 4.3 V, and 4.4 V, for initial five cycles at 0.1C with four successive cycles at each of the following rates: 0.2C, C/3, 0.5C, 1C, and back to 0.1C, with subsequent extended cycling at C/3. Extended cycling, to 50 cycles, was also performed for NMC9055 at a rate of 0.1C between 2.8 V and 4.4 V.

Constant current constant voltage (CCCV) charging. NMC622 and NMC9055 half-cells were charged using a CCCV protocol, with an initial CC charge at a rate of 0.1C until a potential of 4.5 V. The cells were then held at 4.5 V until the current reached a rate of 0.02C, and then were discharged to 2.8 V. Electrochemical impedance spectroscopy (EIS) was performed within a frequency range of 1 MHz–100 mHz with a potential amplitude of 10 mV.

XAS and XPS

Pristine electrode samples were taken from the as-prepared slurry dried on carbon coated aluminum without any exposure to solvent or further processing. Commercial NMC333 (MSE Supplies) was coated on a C/Al current collector following the same methods as described above for NMC622 and NMC9055 to be used as a reference. All cathode samples taken after carefully dissembling the cells were washed with dimethyl carbonate (DMC) and dried in an argon-filled glovebox. *Ex situ* Ni, Co, and Mn L-edge, as well as O, F, and C K-edge soft XAS spectra were collected at beamline 8–2 at Stanford Synchotron Radiation Laboratory (SSRL) under ultrahigh vacuum (10^{-9} Torr) at room temperature using the total electron yield (TEY) and fluorescence yield (FY) detection modes. XPS experiments were performed at the Molecular Foundry with a ThermoFisher K-Alpha Plus XPS/UPS (Al Kα source λ = 1487 eV) and all spectra were calibrated to a C 1s signal of 285 eV. All samples

were measured at two different locations to examine element homogeneity on the electrode. XPS depth profiling experiments were performed at the very surface of each sample, followed by 100 s of etching over that same position, followed by another 100 s of etching, for a total of 200 s of etch time. High resolution bonding spectra for each element of analysis were measured at each subsequent *z*-position before the sample was etched further.

EQCM

An AWSensors EQCM was coupled to a Biologic SP-200 single channel potentiostat. All sensors used in this study were 14 mm AT-cut gold/titanium wrapped 5 MHz quartz crystals, purchased from AWSensors. A proprietary AWSensors electrochemical cell specialized for air-free Li ion experiments was used. The reference and counter electrodes were lithium foil, and the working electrode was an Au/Ti 5 MHz sensor coated with a slurry of active material, carbon nanotubes, and PVDF, in a weight ratio of 8 : 1 : 1. 16 mg of active material (commercial NMC622, NMC811 (MSE Supplies), or NMC9055), 2 mg of carbon, and 2 mg of PVDF were sonicated for 60 minutes with 2 mL of NMP to form an ink. After sonication, the slurry was airbrushed onto the sensor using a Pasche airbrush kit to ensure the sensor was completely covered by a thin layer. The coated sensor was then dried in an oven for 2 h. The mass deposited was measured using the Sauerbrey equation by comparing to the fundamental frequency of the same uncoated sensor and was consistently in the few tens of μg cm^{-2}. Finally, the sensor was transferred into the glovebox, assembled with the AWSensors electrochemical cell, and submerged in 1.4 mL of 2 M lithium bis(trifluoromethanesulfonyl)imide (LiTFSI) in 1 : 1 EC : DMC. The Li air-free holder, along with the sensor and lithium counter/reference electrodes, was transferred out of the glovebox and used for subsequent EQCM measurements. Multiple electrolyte compositions were tested (1 M $LiPF_6$ in 1 : 1 EC : DMC, 2 M $LiPF_6$ in 1 : 1 EC : DMC, 2 M $LiPF_6$ in 3 : 7 EC : EMC, 1 M LiTFSI in 1 : 1 EC : DMC, and 2 M LiTFSI in EC : DMC) to obtain the strongest electrochemical response.

Results and discussion

Electrochemistry

A series of electrochemical measurements for NMC622 and NMC9055 in lithium half-cells were performed in order to explore the differences between the two materials. NMC9055-containing cells cycled between 2.8 V and 4.2 V, 4.3 V, or 4.4 V have initial capacities of 182, 201, and 214 mAh g^{-1}, respectively (Fig. 1a). However, after rate testing (see Experimental section), those capacities decreased, with a higher voltage limit corresponding to a greater capacity fade. Increasing the potential limit to 4.4 V offers little benefit after extended cycling compared with a potential limit of 4.3 V. In contrast, cells with NMC622 can be charged to a voltage up to 4.5 V with limited capacity fade (Fig. 1b). Only when the voltage limit is raised to 4.7 V is there obvious capacity fade for NMC622-containing cells. When charged to 4.3 V, cells with NMC622 have an initial capacity of 167 mAh g^{-1}, which increases to 183 and 191 mAh g^{-1} when charged to 4.4 V and 4.5 V, respectively (Fig. S1). NMC622 also shows slightly more capacity fade associated with a larger voltage window after rate testing (Fig. 1b), though not nearly to the same extent as that of the cell containing NMC9055. At a rate of 0.1C, NMC9055 cells charged to 4.4 V exhibit a significant capacity fade, with only 157 mAh g^{-1} capacity being retained after 50 cycles (75% capacity retention) (Fig. 1c).

The differential capacity (dQ/dV) plots (Fig. 1d, e, and Fig. S1b) provide information about the electrochemical processes involved. In contrast to NMC622, which only shows the H1–H2 phase transition (Fig. S1a), NMC9055 exhibits dQ/dV peaks associated with H1–M (~3.65 V), M–H2 (~3.7 V), and H2–H3 (~4.2 V) phase transitions (Fig. 1d).[15–17] NMC622, which does not show the H2–H3 phase transition in this potential range, does not appear to have significant capacity decay during cycling. However, NMC9055, which does show the H2–H3 transition, shows some capacity fade over the first five cycles at each chosen potential limitation (Fig. 1e). NMC9055 shows significantly more capacity fade as the rate is increased from 0.1C to 1C compared to NMC622 (Fig. S2). At a potential limit of 4.2 V, the H2–H3 phase transition is only partially completed, as shown by the dQ/dV plots for cells cycled to this potential limit. This is consistent with known conclusions, that the H2–H3 phase transition is triggered when charging NMC9055 cells to higher potentials, leading to higher capacities but accompanied by faster capacity fade during cycling.[15,17,18]

CCCV charging was utilized in this study to determine the effect of charging protocol on the capacity fade of NMC9055 cells. With the described testing protocol, NMC622 cells maintained discharge capacities of above 200 mAh g^{-1} for 20 cycles, with an initial capacity of 208 mAh g^{-1} (Fig. 1f). While NMC9055 began with an initial capacity of 217 mAh g^{-1}, by the 20th cycle, it only had 80% capacity retention (174 mAh g^{-1}) (Fig. 1g). CCCV charging for NMC622 provides significantly improved capacities as compared to CC charging. In contrast, NMC9055 does not show improved capacities as a result of either the potential range being increased to 4.5 V, or when CCCV charging is used. In fact, after 20 cycles, CCCV charging to 4.5 V yields worse capacity retention than CC charging to 4.4 V, suggesting that high voltage charging exacerbates electrolyte decomposition and causes capacity fade. EIS measurements were taken on the CCCV cells at the end of discharge for the cycles as indicated in Fig. S3. The total resistance for NMC9055 cells is higher than that of NMC622 cells after a similar number of cycles, consistent with the worse capacity fade observed for the former.

Soft XAS

Soft XAS measurements of the Ni L-edge were taken on both NMC622 (Fig. 2a and b) and NMC9055 (Fig. 2c and d) cathodes. Fig. 2a–d show the L_3 region of the spectra, where splitting into two peaks (L_{3high} and L_{3low}) is evident. The ratio of

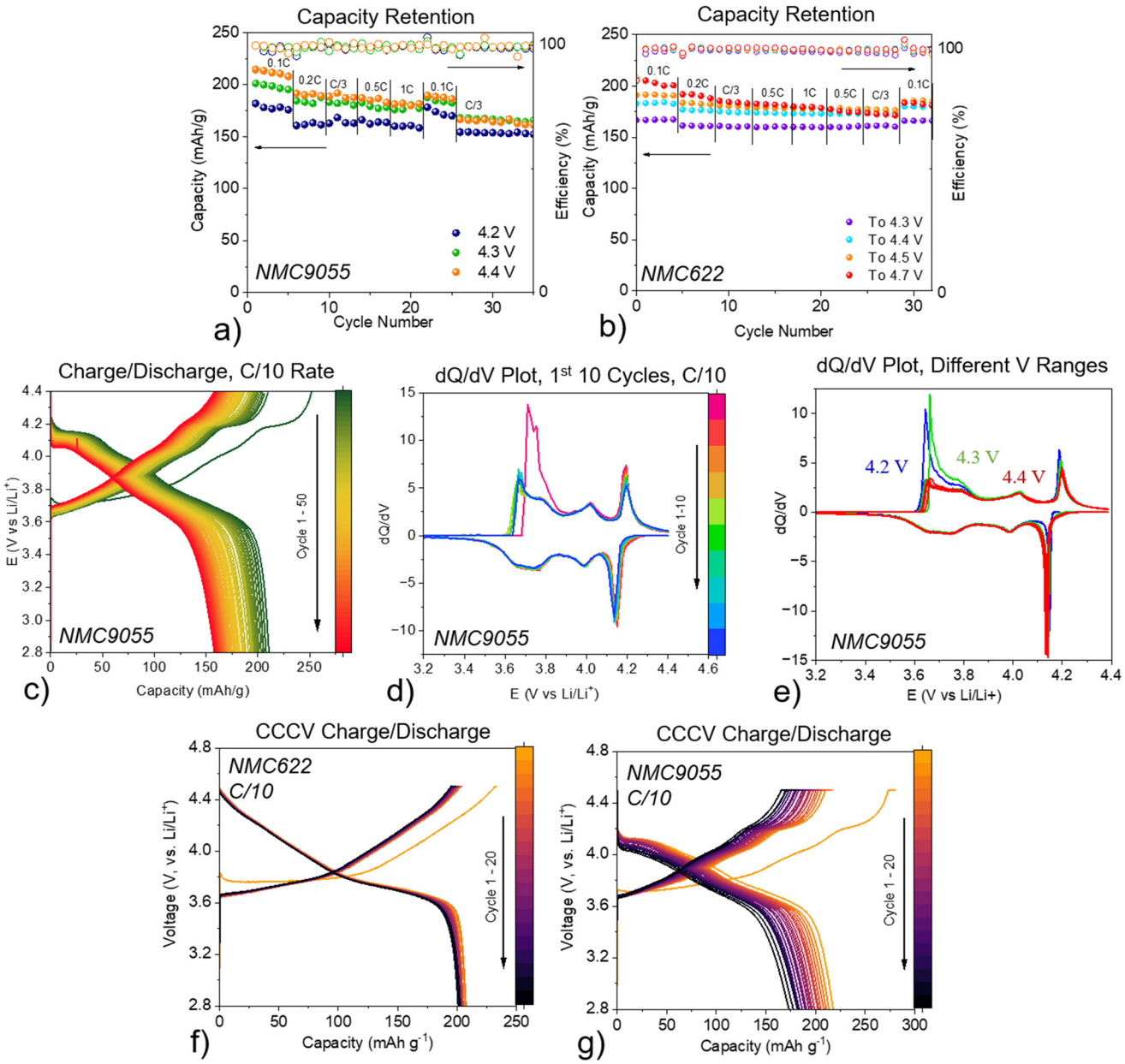

Fig. 1 Rate capacity retention plots at selected cutoff voltages of lithium half-cells containing (a) NMC9055 and (b) NMC622. (c) Charge/discharge plot for the first 50 cycles of a NMC9055 half-cell, between potentials of 2.8 V and 4.4 V, at a CC rate of 0.1C. (d) d*Q*/d*V* plot for the first 10 cycles of a NMC9055 half-cell, between potentials of 2.8 V and 4.4 V, at a CC rate of 0.1C. (e) d*Q*/d*V* plot of the first five cycles, at a CC rate of C/10, at three selected voltage cutoffs (4.2 V, 4.3 V, and 4.4 V) for a NMC9055 half-cell. (f) Charge/discharge plot of a Li/NMC622 cell, using CC charging to a potential of 4.5 V, then holding at CV until the C-rate reached 0.02C (1C is defined as 180 mAh g^{-1}), for the first 20 cycles. (g) Charge/discharge plot of a Li/NMC9055 cell, with CC charging to a potential of 4.5 V and then holding at CV until the C-rate reaches 0.02C (1C is defined as 200 mAh g^{-1}), for the first 20 cycles.

the L_{3high} and L_{3low} peak heights, shown in Fig. 2e, is proportional to the Ni oxidation state, with NMC333 having an oxidation state of +2. Ni in NMC622 shows an increase in oxidation state during charging up to a potential of 4.4 V, above which surface reactions and loss of oxygen cause Ni to become reduced.[3,4,13]

Ni in the pristine NMC9055 cathode is close to the +3 oxidation state, higher than that in NMC622, and both are higher than the +2 oxidation state for Ni in NMC333. During initial charge, Ni^{3+}/Ni^{4+} redox dominates. Ni in NMC9055 at the surface is at a higher oxidation state than Ni in NMC622 at the surface for all cells at all potentials. Similarly, bulk Ni in NMC9055 is at a higher oxidation state than bulk Ni in NMC622 (Fig. 2e). When cells are charged to 4.4 V, Ni becomes progressively more oxidized in NMC622 cathodes both at the surface (TEY) and in the bulk (FY). This is also observed for

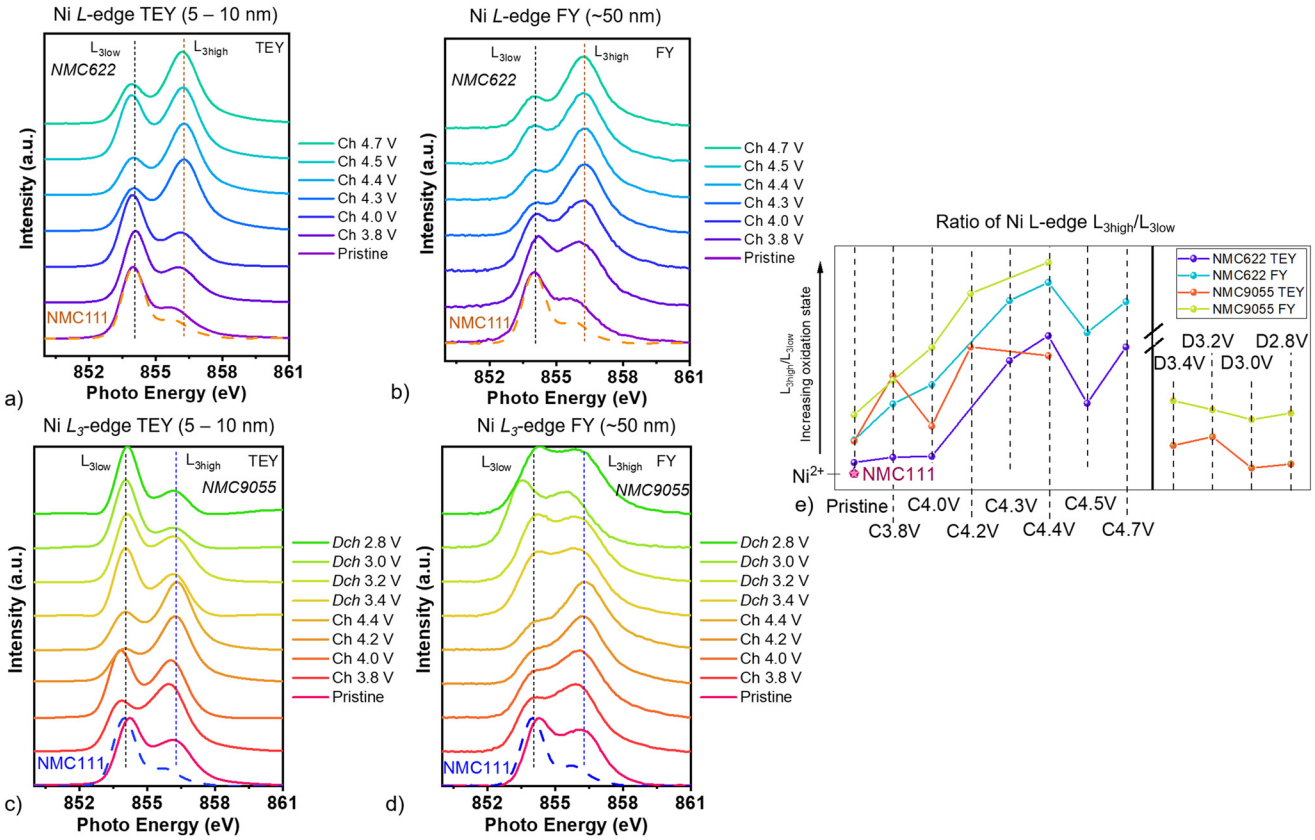

Fig. 2 *Ex situ* Ni L_3-edge in (a) TEY and (b) FY modes of NMC622 cathodes removed from lithium half-cells and cycled to indicated voltage limits. *Ex situ* Ni L_3-edge in (c) TEY and (d) FY modes of NMC9055 cathodes removed from lithium half-cells and cycled to indicated voltage limits. (e) Ratio of Ni L_{3high} and L_{3low} peak heights (L_{3high}/L_{3low}) of NMC622 and NMC9055 cathodes removed from lithium half-cells and cycled to indicated voltage limits.

Bulk Ni (FY) in NMC9055 cathodes. Although Ni in NMC9055 cathodes at the surface also maintains a general trend towards higher oxidation states at higher potentials, Ni in NMC9055 cathodes charged to 4.0 V does not fit this trend, having a lower oxidation state than NMC9055 cathodes charged to 3.8 V. This indicates that a greater nickel content contributes to a higher initial oxidation state in the pristine material and additionally results in more cathode-electrolyte reactions that reduce Ni at the surface during charging, which competes with continuous Ni oxidation upon Li extraction at higher potentials. During the discharge step, for cells discharged to progressively lower potentials down to the end of discharge at 2.8 V, Ni in NMC9055 is at an oxidation state lower than that of the pristine material, but which remains higher than +2. A lower oxidation state for Ni at the surface compared to that in the bulk has been shown for many NMC cathode materials, regardless of composition. Cobalt in the bulk (FY) shows only slight variation in peak position for all measured states of charge in NMC9055 and NMC622 (Fig. S4a–c) (surface cobalt (TEY) of NMC9055 cathode could not be measured with sufficiently good statistics in this investigation due to its low content in the near-surface region).

O K-edge XAS for NMC622 (Fig. S4d) and NMC9055 (Fig. S4e) shows a low-energy, pre-edge region below 535 eV associated with TM 3d–O 2p hybridization, with two distinct peaks for all of the spectra; a broad low energy peak around 530 eV and a higher energy peak at 532.5 eV.[19] Signals from oxygen-containing organic species, such as carbonyls and ketones, which typically form a surface layer that does not penetrate deeper into the bulk, overlap with the latter.[19] Higher-energy peaks at 535 eV and 537 eV represent a combination of carbonate and Li_2O, tentatively ascribed, which also are only detectable at the surface and are present for all states of charging and discharging for NMC9055 (while only being present at low states of charge for NMC622).[20] The ratio of e_g to t_{2g} peak intensity decreased during the delithiation process for both NMC9055 and NMC622. This reflects an increase in unoccupied TM 3d–O 2p orbitals as $Ni^{4+/3+}$–O (and to a lesser extent Co^{3+}–O) are progressively oxidized. Some of the change in the TEY spectra may also be due to consumption of oxygen-containing components during cell charge. In general, a greater Ni content results in a higher Ni oxidation state and concurrently a stronger t_{2g} peak signal, particularly since increasing the overall Ni content increases the covalency of the Ni–O bond, and therefore the intensity of the hybridized TM 3d–O 2p orbitals.[2,3] Ni L-edge XAS showed that Ni deeper into the bulk (measured by FY mode) is at a higher oxidation state than that at the surface (measured by TEY mode). Similarly, O

K-edge XAS shows that the broad t_{2g} TM 3d–O2 p peak at 530 eV has a higher intensity than the e_g peak at 532.5 eV in FY mode. For the cells measured by TEY mode (at the surface), the cells charged to 4.4 V and then discharged to various potentials (3.4 V, 3.2 V, 3.0 V, and 2.8 V) showed a more intense peak at 532.5 eV than at 530 eV, which corresponds to the prevalence of lower oxidation state Ni in the cathode during discharge, though there is also interference from organic oxygen containing compounds at the surface.

F K-edge XAS was performed in order to determine the participation of the electrolyte salt, $LiPF_6$, in the formation of a surface reaction layer for NMC622 (Fig. 3a) and NMC9055 (Fig. 3b). There are no peaks in any of the spectra that can be attributed to transition metal-fluorine bonds, which occur at energies lower than 685 eV.[21] A shoulder located at 690 eV is associated with fluorine in a combination of electrolyte salt $LiPF_6$ and PVDF binder.[22–25] The increased intensity of this peak in the bulk reflects C–F bonds in PVDF, rather than a greater concentration of $LiPF_6$. There is also a peak at 696 eV, which is associated most strongly with $LiPF_6$.[22–25] A peak above 700 eV in some of the NMC622 and NMC9055 spectra can be assigned to Li–F,[22–25] most likely derived from decomposition of the electrolyte salt $LiPF_6$. This peak is not evident in the TEY or FY spectra of the pristine NMC622 electrode but is observed in the spectra of cathodes removed from cells charged to 3.8 V or above, indicating that decomposition

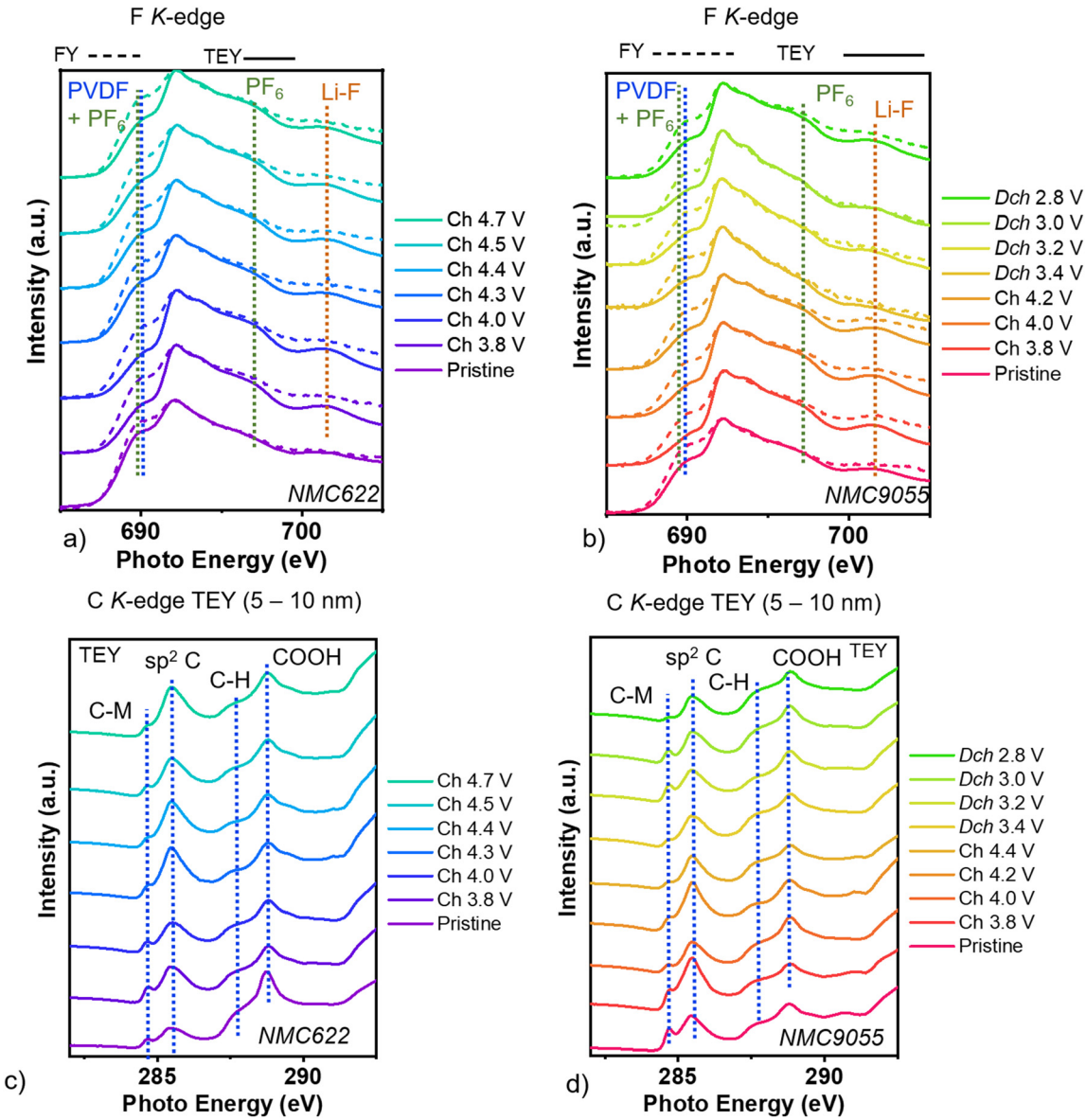

Fig. 3 (a) F K-edge XAS spectra of (a) NMC622 cathodes removed from Li half-cells at the indicated potentials, in TEY mode (straight line) and FY mode (dashed line) and (b) NMC9055, in TEY mode (straight line) and FY mode (dashed line). *Ex situ* C K-edge XAS spectra, in TEY mode for (c) NMC622 cathodes removed from lithium half-cells at the indicated potentials, and (d) NMC9055.

occurs at fairly low potentials. The peaks associated with Li–F are much stronger at the surface, as seen in TEY mode, compared to those in the bulk (FY mode). We did not observe a strong signal associated with PVDF at the surface, and therefore do not believe binder decomposition strongly contributes to the presence of LiF measured by TEY mode.

The F K-edge spectra of the NMC9055 electrodes shows similar trends to those of NMC622. NMC9055 also has peaks associated with PVDF, $LiPF_6$, and Li–F at 690, 696, and above 700 eV, respectively. As with NMC622, the peak at 690 eV for NMC9055 is stronger when measured by FY mode (deeper into the bulk) as compared to at the surface (measured by TEY mode), primarily attributable to PVDF in the composite electrode. Signals due to LiF above 700 eV are evident in both the TEY and FY spectra of charged NMC9055 cathodes. This indicates that electrolyte decomposition occurs more aggressively for NMC9055, and the decomposition products penetrate more deeply into the bulk of the NMC9055 cathode than for NMC622.

Carbon K-edge XAS, measured *ex situ* at the surface in TEY mode, shows spectral changes indicating a dynamic surface evolution of carbon-containing species during charging and discharging (Fig. 3c and d). Both NMC622 (Fig. 3c) and NMC9055 (Fig. 3d) show distinct peaks throughout the pre-edge region (at energies lower than 292 eV). At peak energies around 285 eV, signals are associated with double bonded carbon–carbon like sp^2 carbon.[26] At energies of 287 eV–290.5 eV, various carbon functionalities can contribute where generally the peak position reflects the electronegativity of the local carbon environment.[26] For NMC622 and NMC9055, the strongest peaks at 287.8 and 288.8 eV can be attributed to C–H and COOH, respectively.[26] Note that all cathodes were washed with dimethyl carbonate prior to measurement and dried inside a dry glove box. Additionally, these XAS measurements were performed under ultrahigh vacuum, limiting the effects of remaining solvent. The presence of COOH by carbon K-edge XAS indicates reacted surface carbonate for both NMC9055 and NMC622. A shoulder at 284 eV is present at all C 1s K-edge spectra taken at all points during charging and discharging for NMC9055, and has been identified to arise from interactions between hybridized TM–Csp^2 orbitals.[26–28] It is present on low-voltage NMC622 cathodes as well, though with lower peak intensities. This initial shoulder peak was also observed in samples of graphene and other conductive carbons grown on transition metal catalysts and complexed with the carbon.[26–28] Therefore, measured NMC622 and NMC9055 cathodes also appear to show organometallic carbon-TM complexes. Carbon measured by XAS deeper into the bulk, in FY mode, shows a far weaker signal than at the surface (Fig. S5). C K-edge XAS in FY mode for both NMC622 and NMC9055 shows peaks primarily comprised of carbon–carbon interactions.

XPS

The C 1s XPS spectra of NMC622 and NMC9055 cathodes removed from lithium half-cells at various states-of-charge are shown in Fig. 5a and b, respectively. The penetration depth of these experiments is about 50–100 Å. The very surface of each cathode is covered with many organic species, including C–O, C═O, CO_3^{2-}, and $-CF_2$ functional groups.[1,29] Soft XAS showed that Ni at the surface, at approximately 5 nm depth, is at a lower oxidation state than deeper into the bulk. It is therefore possible that this lower surface oxidation state is due to covalent interactions between electron-rich CEI products and Ni orbitals, and that higher Ni content increases the strength and covalency of these interactions. Bonds related to TM–C, in

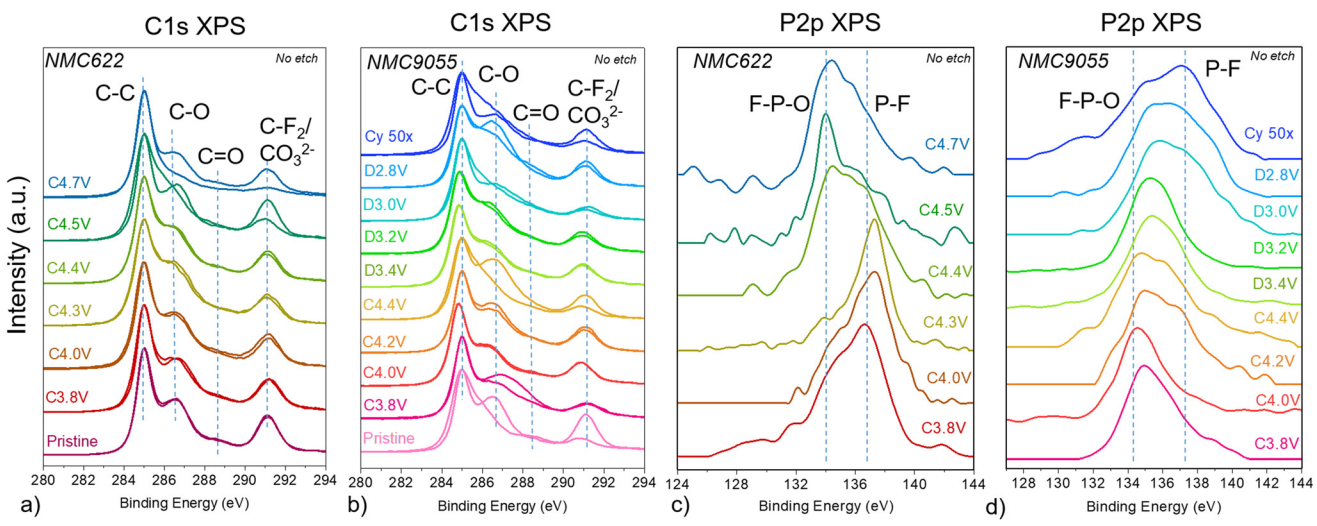

Fig. 4 (a) *Ex situ* C 1s XPS for NMC622 and (b) C 1s XPS for NMC9055 cathodes, removed from lithium half-cells at the indicated potentials. Two spots were measured on each cathode to account for non-homogenous organic signals. Dashed guidelines represent binding energies of common carbon signals; P 2p XPS for (c) NMC622 and (d) NMC9055 electrodes removed from lithium half-cells, at the indicated potentials. Dashed guidelines represent common P binding energies.

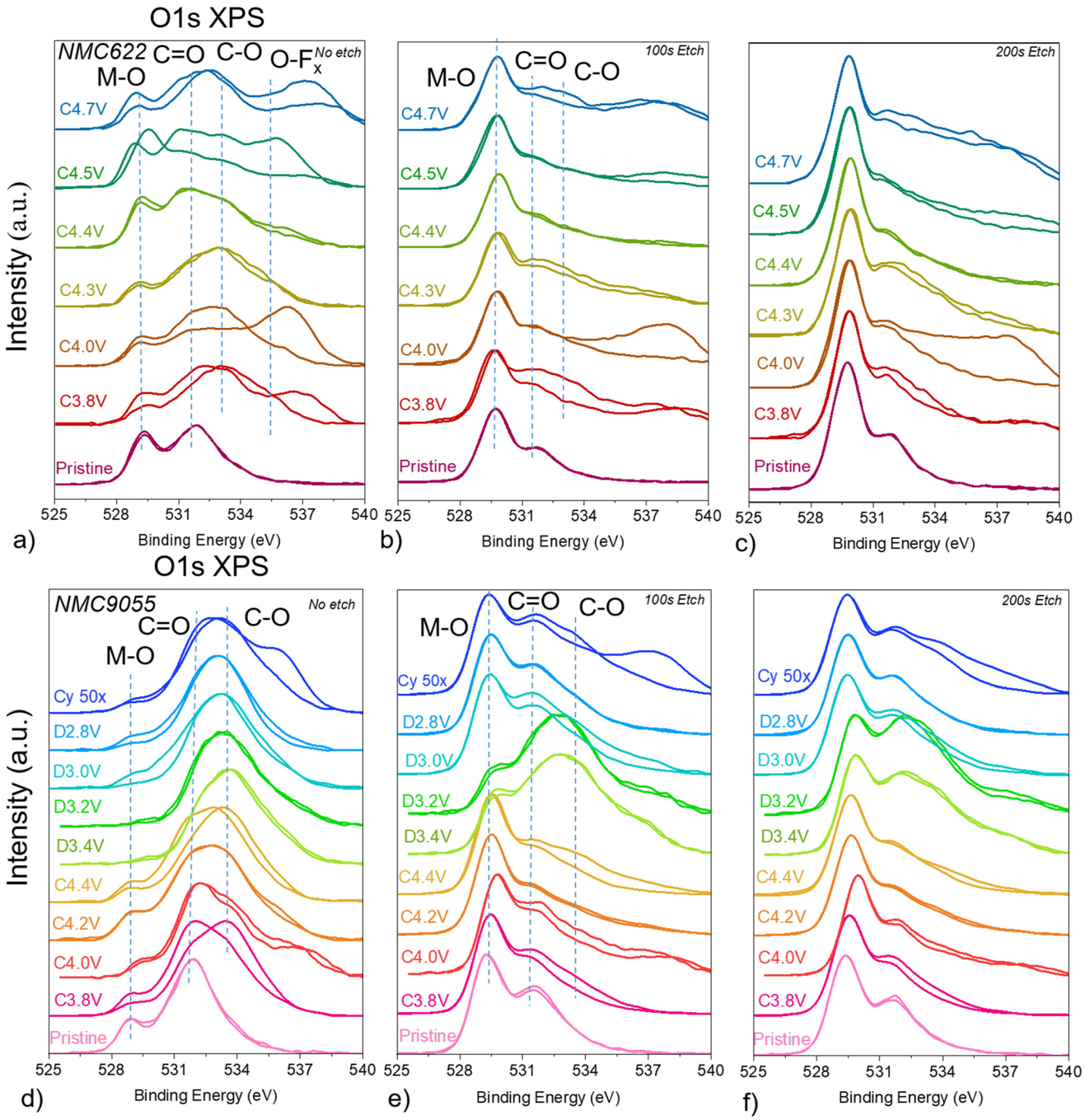

Fig. 5 *Ex situ* O 1s XPS spectra for NMC622 cathodes removed from lithium half-cells at the indicated potentials: (a) no etching (b) 100 s etching and (c) 200 total seconds of etching over the same spot. Two spots were measured on each cathode to account for non-homogenous organic signals. *Ex situ* O 1s XPS spectra for NMC9055 cathodes removed from Li half-cells at the indicated potentials: (d) no etching (e) 100 s etching and (f) 200 total seconds of etching over the same spot. Dashed guidelines represent common O 1s binding energies.

particular Ni–C, are found at energies from 283–285 eV, and can therefore be difficult to deconvolute from organic carbon bonds. However, it is possible that particularly broad peaks centered around 285 eV have contributions from TM–C bonds. NMC9055 C 1s XPS spectra show broader peaks, which corroborates the relatively stronger TM–C signals for NMC9055 cathodes shown by C K-edge sXAS. All XPS spectra were normalized to adventitious carbon peak at 285 eV, and each cell at a particular potential was measured at two different spots in order to track localized CEI formation. For NMC622 cathodes, the CEI formation appears fairly homogenous up to a potential of 4.4 V, indicated by the overlap of two spectra collected in different spots. At higher potentials (≥4.5 V), however, the two spectra do not match well. The intensity of the C–O peak at

286.5 eV decreases at highly charged states, indicating the evolution of the CEI during charging. In comparison, the CEI layer is less homogenous for most NMC9055 cathodes at various states-of-charge, as evidenced by the differences in the two spectra taken on different spots. There are also more changes in the spectra as a function of state-of-charge of the electrode compared to NMC622. For example, in addition to a strong C–O bond at 286.5 eV, an increased C═O signal at 288.7 eV appears for the electrodes taken from cells charged to 3.8 V, 4.4 V, and charged to 4.4 V and then discharged to 2.8 V. These differences indicate a greater surface instability for NMC9055 as compared to NMC622, and greater participation of the CEI during cell charge and discharge, as surface organics are readily consumed and deposited. These layers are very thin based on depth profiling experiments. After just 100 seconds of etch time, all of the CEI-related peaks disappear for both the NMC622 and NMC9055 cathodes, and the only peaks remaining are C–C conductive carbon bonds at 285 eV and C–F bonds from PVDF at 291 eV (Fig. S6). As with the C K-edge sXAS results, there are no possible TM–C signals measured deeper into the bulk, indicating that it is purely a surface phenomenon.

P 2p XPS was used to track electrolyte decomposition during charging and discharging of NMC622 (Fig. 5c) and NMC9055 (Fig. 5d) electrodes in lithium half-cells. The electrolytic solution used in the cells was $LiPF_6$ in EC/DEC. A shift from P–F at 138 eV (as is native in $LiPF_6$) to F–P–O at 134 eV would indicate that $LiPF_6$ is reacting with decomposed electrolyte solvent in the cell. At the very surface, P that has been deposited from the electrolyte salt on NMC622 composite cathodes is primarily detected in the form P–F for cells that have been charged to potentials up to 4.3 V. In electrodes taken from cells charged to higher potentials (4.4 V–4.7 V), however, a lower energy signal associated with F–P–O began to dominate the XPS spectra. In contrast, NMC9055 cathodes show a strong F–P–O signal even when charged to just 4.0 V in half-cells, which remains strong at all states-of-charge. A signal from P–F reappeared on cathodes taken from cells that were charged to the end of charge as well as in cathodes taken from cells discharged to the end of discharge after charge to 4.4 V, indicating either dissolution of F–P–O species, revealing buried pristine salt underneath, or deposition of more PF_6^- onto the cathode. After 50 cycles, at the end of discharge, it is clear that P–F containing compounds have accumulated on the cathode upon cycling. The appearance of F–P–O peaks at earlier states-of-charge for NMC9055 than NMC622 indicates that a higher oxidation state, facilitated by charging to higher potentials but also found in Ni-rich NMCs, can be correlated with decomposition of LiPF6. Indeed, while the measured oxidation states of both NMC622 and NMC9055 at the very surface by sXAS show interactions with surface oxygen, NMC9055 appears to have a similar oxidation state at 4.2 V as NMC622 at 4.4 V, suggesting this decomposition could well be oxidation-state dependent.

Depth profiling XPS experiments were performed for NMC622 and NMC9055 electrodes (Fig. S7). For NMC622, there was only measurable signal from phosphorus after 100 s of etching. For NMC9055, there was measurable signal from P 2p XPS after two rounds of etching, each for 100 s (the second amounting to 200 total seconds). The P 2p spectra of the etched samples were similar to those at the surface, and thus this indicates that NMC9055 electrolyte salt penetrates deeper into the cathode than electrolyte salt in NMC622, possibly infiltrating due to the formation of microcracks formed during cycling of NMC9055 cathodes.[6–9] This corroborates the F K-edge XAS data presented previously, which showed electrolyte salt decomposition product LiF by both TEY mode at the surface as well as by FY mode, into the bulk.

O 1s XPS of NMC622 reveals that, at the very surface (Fig. 4a), organic oxygen containing species dominate, such as those containing C═O (including carbonate) at 531.6 eV, C–O at 532.5 eV, and O–F_x at ~535 eV.[12,29,30] The intensity of the peak at 529.5 eV grew in cathodes taken from cells charged to progressively higher potentials. This peak likely represents lattice oxygen because it does not change position across cathode samples or with etching, though the influence of Li_2O (which appears at similar binding energies to lattice oxygen) might be responsible for observed deviations at high potentials. TEY mode of O K-edge sXAS of NMC622 cathodes indicated that Li_2CO_3 was consumed as the cell was charged. This causes evolution of gaseous CO_2 and Li_2O left on the surface as a decomposition product. Surface Li_2CO_3 consumption, exposing buried lattice oxygen, as well as Li_2O left as a decomposition product are both responsible for the increase in the M–O signal at 529.5 eV. This may also explain an anomalous peak at 537 eV, which has been previously ascribed to adsorbed gases such as O_2 and CO_2, and which appears primarily on cells charged to potentials where Li_2CO_3 decomposition is noted.[31–34] When the cathodes are etched for 100 s, measured, and then etched for another 100 s (200 s total) to perform depth profile measurements (Fig. 4b and c), the metal–oxygen signal dominates, indicating as with C 1s XPS that the CEI is very thin, on the order of a few Å. The anomalous high-energy peak remains for the cells charged to 4.0 V and 4.7 V even after 200 s etching.

Similar to the case with the NMC622 electrodes, O 1s XPS taken on NMC9055 electrodes charged to various potentials shows that signals from organic oxygen containing compounds dominate at the very surface (Fig. 4d). These are primarily in the form of C═O and C–O, at 531.6 and 532.5 eV, respectively. At the very surface, although peaks associated with organic oxygen containing species dominate, there is still measurable signal from lattice oxygen for electrodes measured at all states-of-charge. Because lattice signals are visible even at the very surface, the CEI is either thinner than the probing depth, or is nonhomogenous and has incomplete coverage of the cathode surface. However, the lattice oxygen signal at all measured states is weaker than that observed in the O 1s XPS spectra of NMC622 electrodes, indicating the formation of a thicker layer of surface organic species on NMC9055 electrodes. Particularly, for all states-of-discharge in NMC9055, the lattice oxygen signal is weak to nonexistent, indicating that during discharge there is a greater concentration of surface

organics. This is shown by O K-edge sXAS as well (Fig. S4), where TEY mode measurements of NMC9055 cells taken at various states of charge show pre-edge peaks at 529 eV, associated with t_{2g} TM 3d–O 2p hybridized orbitals, and 531 eV, associated with carbonyl signals and e_g TM 3d–O 2p orbitals. However, NMC9055 electrodes measured at various states-of-discharge showed very weak to nonexistent TEY signals at 529 eV, with carbonyl signals at 531 eV dominating. O K-edge sXAS shows peaks, measured in TEY mode, associated with Li_2CO_3 on NMC9055 cathodes at low potentials. However, at the end of charge, at a potential of 4.4 V, the Li_2CO_3 signal is weaker. This is corroborated by O 1s XPS findings, where the binding energy of the broad peak shifts higher, from a position attributable to sp^2 carbon–oxygen bonds (including carbonate) in cells charged to lower potentials, to a position associated with sp^3 carbon–oxygen bonds in NMC9055 cathodes charged to higher potentials. During discharge, the binding energy measured by O 1s XPS shifts back to values associated with sp^2 carbon–oxygen signals, including carbonate. As with the NMC622 electrodes, after 100 s etch time, the M–O signal at 529 eV dominates for all the electrodes except for those discharged to 3.4 V and 3.2 V (Fig. 4e). Those spectra appear to still be dominated by C═O and C–O signals, which implies the CEI layer is thicker on these electrodes (Fig. 4f). The initial charging process for NMC622 appears to show clear consumption of surface compounds, in particular Li_2CO_3. While NMC9055 shows consumption of carbonyl-containing compounds during charge, it also indicates high-potential redeposition of compounds containing C═O moieties. Therefore, the behavior of Li_2CO_3 is highly dependent on Ni content, making Li_2CO_3 one of the key species for understanding cathode surface layers.

The XPS spectra of transition metals in NMCs are complicated by the interference of satellite peaks at binding energies associated with TM XPS. Fluorine from the binder or decomposed electrolyte salt emits an auger electron upon core–shell excitation, the F_{KLL} peak, which appears at 860 eV when an Al X-ray source is used for XPS measurements; this overlaps with the Ni 2p XPS spectra.[35,36] Both NMC622 and NMC9055 at the very surface with no etch time show what is likely interference from this F_{KLL} peak in their Ni 2p spectra (Fig. 6a and d). While this complicates the Ni 2p XPS spectra, it provides additional information about the CEI. For NMC622 cells, the F_{KLL} peak shrinks above potentials of 4.4 V, the same potentials at which the P 2p signal is dominated by electrolyte decomposition products containing O–P–F and O–P moieties. The Ni 2p XPS shows a greater signal at 855 eV, typical for layered nickel oxides.[37] This indicates that there is a connection between electrolyte salt decomposition and consumption of surface organic compounds, which then exposes the surface of the NMC. After 100 s and 200 s of etching, the F_{KLL} peak is far weaker and Ni XPS of each cell shows the strongest peak at 855 eV, which remains stable throughout charging to 4.7 V (Fig. 6b and c).

The Ni 2p XPS spectra for NMC9055 is very similar to that of NMC622, with XPS measurements taken at the very surface showing the F_{KLL} peak at 860 eV (Fig. 6d). Unlike in NMC622, this signal remains throughout charging, discharging, and cycling 50×; it is not consumed as the surface layer for NMC622 is. However, just as with NMC622, after 100 s of etch time, XPS measurements of Ni on the NMC9055 cathode show the peak position has shifted to 855 eV (Fig. 6e). This is true for all charging and discharging points, except for those representing the cathode discharged to 3.4 V and 3.2 V, which show the fluorine-containing surface layer penetrating deeper into the bulk (Fig. 6f).

There was no Co XPS signal at the surface for either NMC622 or NMC9055 electrodes. After 100 s of etching, both showed Co signals. While both NMC9055 and NMC622 XPS spectra show a Co peak at 782 eV, NMC9055 additionally shows a low-energy shoulder peak at 775 eV, both of which are typical of cobalt oxides (Fig. S8).[38] However, as with the F_{KLL} peak, Al Kα X-rays as the excitation source for XPS result in a Ni_{LMM} peak at 775 eV.[35,36] The intensity of this Ni_{LMM} peak is related to the relative proportion of Ni in the cathode, and as such NMC9055 shows a stronger Ni_{LMM} signal than NMC622 interfering with Co XPS spectra. Similar phenomena occur for Mn 2p XPS of NMC9055 and NMC622, which is expected to be entirely electrochemically inert during cycling. The Mn 2p XPS spectra of NMC622 has a peak maximum at 642 eV, similar to that of MnO_2 (tetravalent Mn).[39] This is the case for all the NMC622 cathodes regardless of state-of-charge, and at all three etch levels (Fig. S9). Mn did not have a measurable signal at the surface of NMC9055, but peaks emerged after etching the cathodes for 100 and 200 s. Instead of one peak at ~642 eV and a smaller, satellite peak at 654 eV, typical of Mn^{4+}, NMC9055 showed one very broad peak that spanned the energy range within 635 and 650 eV (Fig. S9). Peak broadening and distortion are associated with improperly compensated charging effects in insulating samples.[40,41] This might indicate a localized buildup of charges for Mn in the NMC9055 lattice. A Ni_{LMM} peak is also expected to occur at 638 eV, which would cause peak broadening in the Mn XPS spectra.[36] It is likely both of these factors contribute to the anomalously broad Mn XPS signal in NMC9055. Despite this, Mn still appears electrochemically inert (its peak shape/position does not change at all during charging or discharging).

EQCM

EQCM is a versatile technique that can be used to investigate surface properties in Li ion cells *in situ*. EQCM operates by measuring the resonant frequency of a quartz crystal simultaneously with the electrochemical current response, and its underlying principle is based on the Sauerbrey equation.[42–44] The gravimetric response to electrochemical measurements will be reflected by a change in the oscillating frequency of the quartz crystal sensor, following the relation:

$$\Delta f = -C_f \Delta m,$$

where C_f is the sensitivity factor of the quartz crystal; 17.7 ng $(cm^2\ Hz)^{-1}$ for the 5 MHz crystals used in this measurement. The Sauerbrey equation can be combined with Faraday's law for a relationship that is useful for battery mechanism studies, the mass per mole of electrons (MPE);[45–49] that is, the mass change on the quartz crystal sensor per mole of electrons passed during the electrochemical measurement. For example, if the mpe is

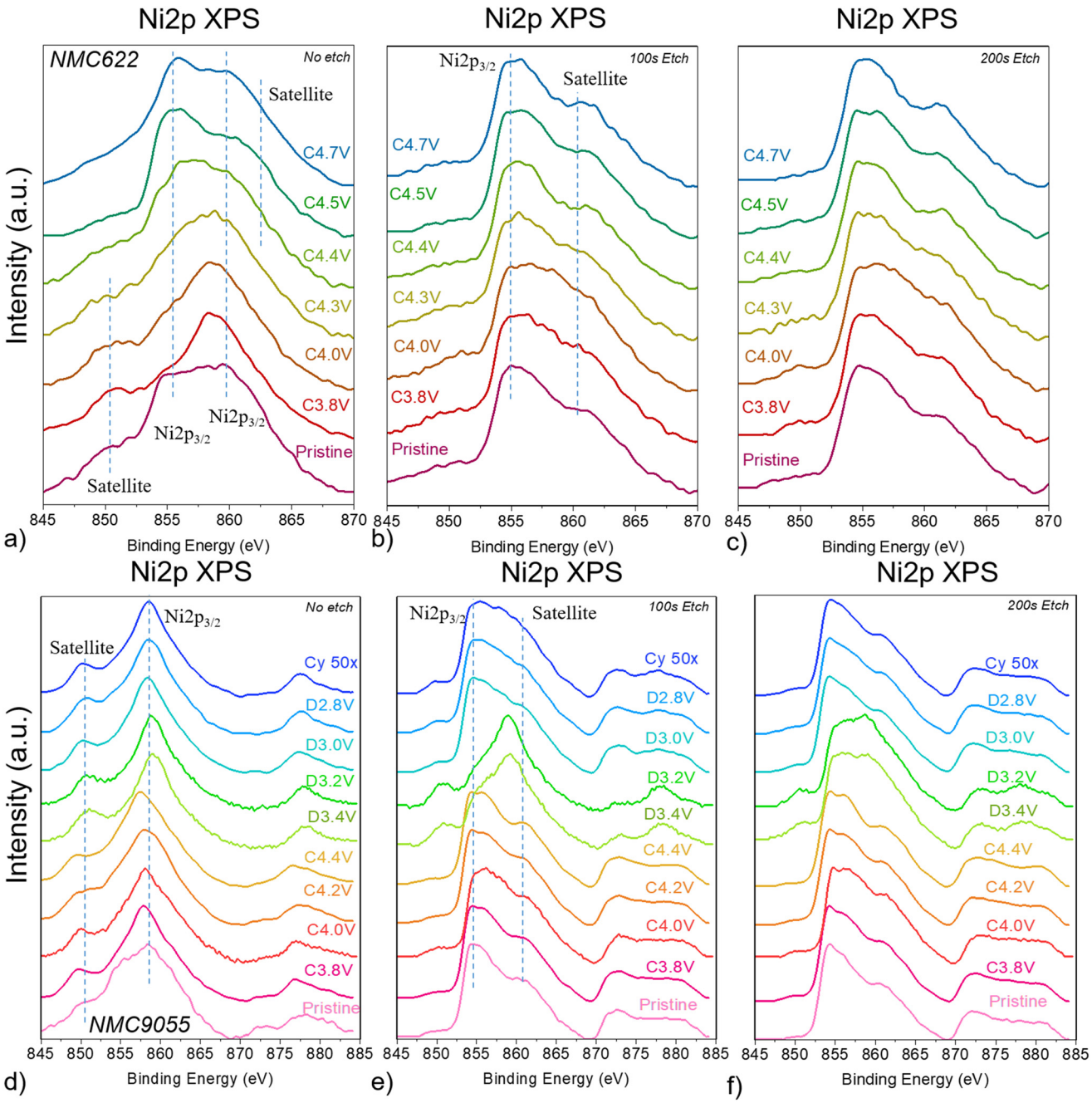

Fig. 6 *Ex situ* Ni 2p XPS spectra for NMC622 cathodes taken from lithium half-cells at the indicated potentials: (a) no etching (b) 100 s etching and (c) 200 total seconds of etching over the same spot and for NMC9055 cathodes: (d) no etching (e) 100 s etching and (f) 200 total seconds of etching over the same spot. Dashed guidelines represent common Ni binding energies.

approximately ±6.94 g mol^{-1} e^{-}, it can be extrapolated that one Li ion is deposited/extracted during a particular electrochemical response. The combined equation is as follows:

$$\mathrm{MPE} = -nC_{\mathrm{f}}F\frac{\Delta f}{Q}$$

When the equation is rearranged, it becomes clear that by plotting the charge (current multiplied by time) *versus* the change in frequency, the slope of the line can be used to determine the MPE value between any two potentials. In order for the Sauerbrey equation to be considered an appropriate relation, we must determine whether $\Delta f/f_0 < 2\%$, meaning the change in frequency (Δf) caused by adding a surface slurry film divided by the fundamental frequency of the quartz crystal (f_0) must be <2%. This was determined for all deposited films prior to further analysis.

In addition to NMC622 and NMC9055, NMC811 was examined as well. Because of the lack of EQCM data on NMC com-

pounds, adding NMC811 allows for more robust comparison and creates a greater library of EQCM data available for NMCs.

Cyclic voltammetry (CV) was also recorded for a sensor with a surface film consisting of only carbon and PVDF. This showed very low current response and no electrochemical peaks (Fig. S10). CVs of EQCM cells with NMC slurries in the chosen EQCM solvent system are very similar to the CVs taken of coin cells containing NMC cathodes in a typical NMC electrolyte system (1 M $LiPF_6$ in 1 : 1 EC : DEC) (Fig. S11).

The initial CVs of three electrode EQCM cells containing NMCs (Fig. 7a–c) differ somewhat from later cycles. All three NMCs have an intense oxidation peak as the CV potential is swept from 3.0 V to 4.4 V (or 4.5 V in the case of NMC9055). NMC622 and NMC811 have their initial oxidation peak centered at approximately 4.15 V, with NMC9055 slightly more polarized to a potential of slightly above 4.2 V. All three NMCs also show similar behaviors, with either no (NMC9055) or slight (NMC622 and NMC811) mass decrease until the onset of the oxidation peak, after which the mass decreases at a much faster rate. On the discharge potential sweep, from 4.4 V (or 4.5 V) to 3.0 V, both NMC9055 and NMC811 show two pronounced reduction peaks at approximately 4.0 and 3.65 V and one reduction peak is observed at ~3.5 V for NMC622 (Fig. 7a–c). In all cases, surface mass density decreases to different extents until the potential associated with the onset of the first reduction peak is reached. At this potential, both NMC9055 and NMC622 show an increase in surface mass density until the end of discharge. NMC811, on the other hand, shows a mass increase for the first reduction peak, a mass decrease for the second reduction peak, and a mass increase from the end of reduction until the end of discharge.

Charge *vs.* Δm plots were created separately for the initial charge, and then the initial discharge, of all three NMCs (Fig. 7d–i). There are distinct linear regimes, associated with a voltage range on the simultaneous current/frequency change response, which can be used to determine the change in mass associated with one mole of charge passed. The first MPE value for all three NMCs occurs at approximately 4.0 V upon

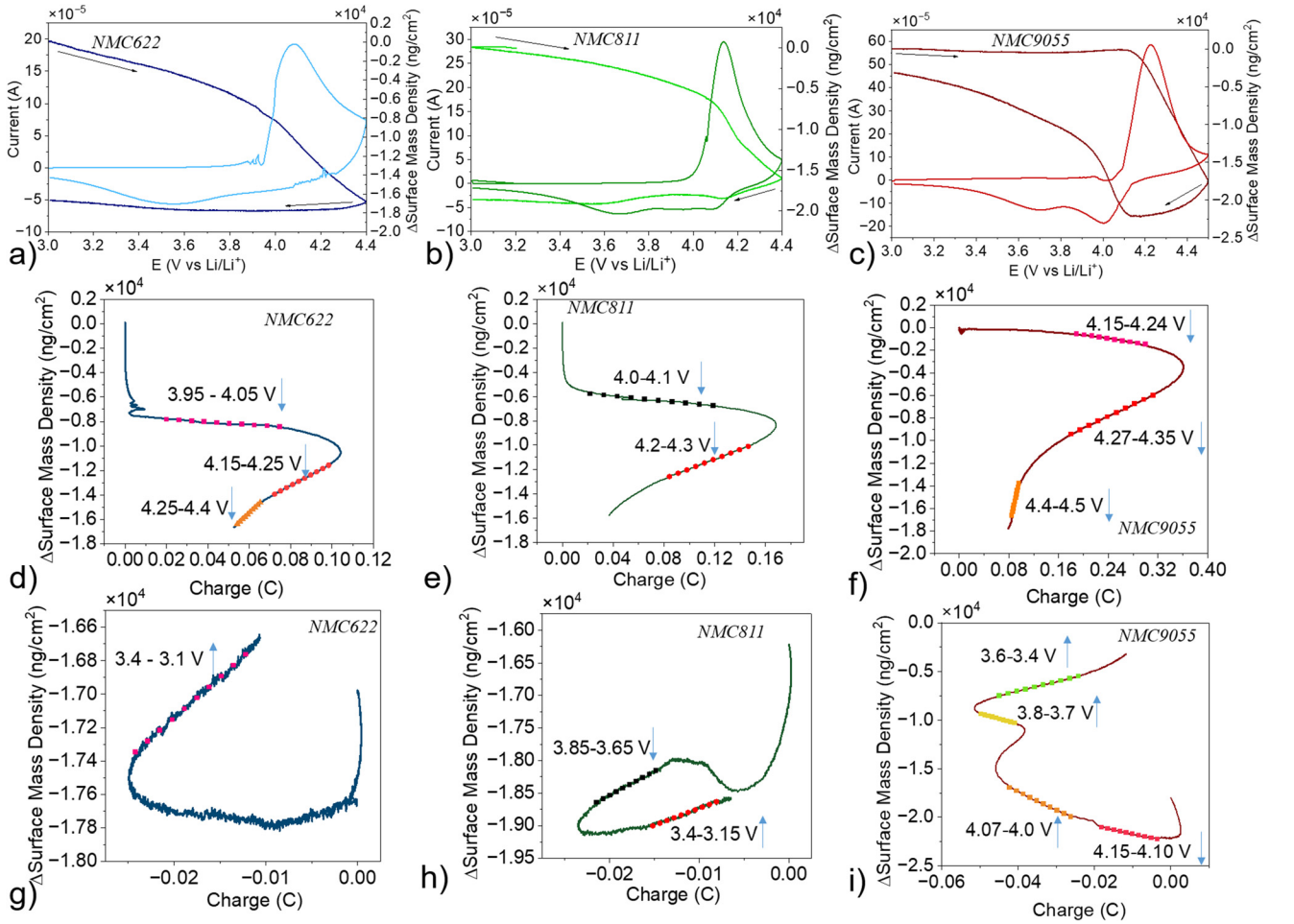

Fig. 7 First-cycle CV and simultaneous surface mass density change of (a) NMC622 (b) NMC811 and (c) NMC9055 in three electrode EQCM cells. Initial oxidation step (from 3.0 V to 4.4 V) charge *versus* surface mass density change for (d) NMC622 (e) NMC811 (f) NMC9055 in three-electrode EQCM cells (down arrows represent a mass decrease in a given potential range). Initial reduction step (4.4 V to 3.0 V) charge *versus* surface mass density change for (g) NMC622 (h) NMC811 (i) NMC9055 in three-electrode EQCM cells (up or down arrows represent a mass increase or decrease in a given potential range, respectively).

Table 1 MPE values during the initial charge and discharge for NMC622, NMC811, NMC9055 in three electrode EQCM cells and the associated voltage range at which they occur. A negative MPE value refers to a decrease in mass; a positive MPE value refers to an increase in mass

Material	Voltage range	MPE (g mol^{-1})
NMC622	*Charge*	
	3.95–4.05 V	−1.6
	4.15–4.25 V	−13
	4.25–4.4 V	−24
	Discharge	
	3.4–3.1 V	+7.3
NMC811	*Charge*	
	4.0–4.1 V	−1.5
	4.2–4.3 V	−5.8
	Discharge	
	3.85–3.65 V	−11
	3.4–3.15 V	+7.7
NMC9055	*Charge*	
	4.15–4.24 V	−1.3
	4.27–4.35 V	−3.8
	4.4–4.5 V	−36
	Discharge	
	4.15–4.10 V	−12
	4.07–4.0 V	+28
	3.8–3.7 V	+16
	3.6–3.4 V	+14

charge. It represents a mass decrease occurring simultaneously with an oxidative current response (Table 1). The absolute values are much smaller than 7 g mol^{-1} e$^-$, implying that the mass loss during oxidation is either primarily driven by chemical decomposition as opposed to electrochemical, or is due to competing effects of simultaneous deposition and dissolution which occur on the sensor surface.[48–50] If deintercalation is simultaneous with deposition on the electrode surface, this would result in an lower |MPE| than expected. At higher potentials, MPE values are more similar to those associated with organic compounds being stripped. EQCM cannot specifically identify which products are being stripped at high potentials, but possibilities based on the reported MPEs of 24 g mol^{-1} e$^-$ for NMC622 and 36 g mol^{-1} e$^-$ for NMC9055 include CO_2 (22 g mol^{-1} e$^-$), LiOH (24 g mol^{-1} e$^-$), LiF (26 g mol^{-1} e$^-$), CH_3OLi (38 g mol^{-1} e$^-$), and Li_2CO_3 (37 g mol^{-1} e$^-$).[48,49] O 1s XPS and O K-edge sXAS experiments on NMC9055 and NMC622 electrodes indicate carbonate being consumed during charging. While NMC9055 shows a mass decrease associated with complete loss of Li_2CO_3, NMC622 shows a mass loss that could be connected to decomposition of Li_2CO_3 into its constituents: gaseous CO_2, which is released, and remaining deposited Li_2O. This was already hypothesized due to peaks appearing in the O 1s XPS spectra of NMC622 cathodes, which showed possible gas adsorption and Li_2O deposition. EQCM provides supporting evidence for the importance of Li_2CO_3 in cathode surface layers, as well as the effect of Ni content on its behavior.

MPE calculations were also determined for the initial reduction of NMC622, NMC811, and NMC9055 after charge in lithium half-cells, from 4.4 V–3.0 V (or 4.5 V–3.0 V for NMC9055). NMC622 only had one linear regime in its charge *vs.* Δm plot, in a potential range of 3.4 V–3.1 V, with a MPE value of 7.3 g mol^{-1} e$^-$ (Fig. 7g), close to what is expected for lithium intercalation without interference from stripping or formation of surface reaction layers. Discharge processes for NMC811 and NMC9055 cells are more complex and show multiple regions from which MPEs can be extracted (Fig. 7h and i). At higher potentials, corresponding to the beginning of discharge, the MPEs are negative (Table 1), suggesting loss of surface species formed from parasitic reactions. An MPE value close to +7 is obtained below 3.4 V in the case of NMC811, as is expected for lithium intercalation without complications from surface layer formation or stripping. In contrast, MPE values much larger than +7 are calculated for NMC9055 below 4.07 V in several voltage regimes, suggesting continuous formation and deposition of surface species in addition to lithium intercalation. The possibly relevant species are Li_2O (15 g mol^{-1} e$^-$), LiF (26 g mol^{-1} e$^-$), or other unidentified components.[48,49,51] This is consistent with the observation of an increased LiF signal measured by F K-edge sXAS on NMC9055 cathodes as cells are progressively discharged as well as the O 1s XPS showing a notably stronger signal associated with C–O and C═O after etching than with the other cathodes.

After the initial cycle, the EQCM cells were cycled three times between 3.0 V and 4.4 V, and the frequency responses were recorded. The MPE results are presented in Table 2. The CVs of all the NMCs stabilized starting from the 2nd cycle (Fig. 8a–c). All three NMCs showed a shift in the change in surface mass density from the 2nd cycle to the 4th towards more negative values. Reasons for this phenomenon require further probing; as such, while MPE values for all four cycles are presented, only those for cycles one and two are discussed in depth.

The charge *vs.* Δm plots for the oxidation of all NMCs are similar during the initial cycle and the subsequent cycles (Fig. 8d–f). The initial linear regime is still associated with mass loss due to oxidation, and the MPE values tend to be slightly less negative as the Ni content increases (Table 2). At higher potentials, the MPE values for NMC622 and NMC9055 become more negative than the MPE values at lower potentials, suggesting more dissolution or electrochemical decomposition of surface species, as in the initial formation cycle. As before, the MPE values could correspond to loss of Li_2O, LiOH, LiF, or CO_2.[49] The higher potential MPEs of NMC811, on the other hand, show a mass *increase* of 4.2 g mol^{-1} e$^-$ which occurs over the same potential range as the second oxidation peak. This value implies multiple competing deposition and dissolution reactions happening at the surfaces, with deposition ultimately being slightly more favored at potentials of 4.15–4.25 V due to this second oxidation reaction.

The MPE values calculated from the reduction step of cycles 2–4 are also similar to those obtained for the initial cycles (Fig. 8g–i). These values in the ranges of 3.5–3.0 V for NMC622 and 3.4–3.15 V for NMC811 are consistent with Li^+ insertion without competing deposition or stripping processes. At higher potentials (corresponding to the beginning of discharge) NMC622 shows only MPE values associated with mass gain, while NMC811 shows MPE values associated with

Table 2 MPE values of NMC622, NMC811, NMC9055 in three electrode EQCM cells during Cycle 2 to 4

Material	Cycle	Voltage range	MPE (g mol^{-1})	Material	Voltage range	MPE (g mol^{-1})	Material	Voltage range	MPE (g mol^{-1})
NMC622	2	*Charge*		NMC811	*Charge*		NMC9055	*Charge*	
		4.0–4.2 V	−4.9		3.7–3.8 V	−4.5		3.75–3.9 V	−4.4
		4.2–4.25 V	−17		4.15–4.25 V	+4.2		4.0–4.1 V	−22
		4.25–4.4 V	−23					4.2–4.4 V	−31
	3	*Charge*			*Charge*			*Charge*	
		4.0–4.2 V	−3.7		3.7–3.8 V	−3.9		3.75–3.9 V	−5.7
		4.2–4.25 V	−10		4.15–4.25 V	+7.3		4.0–4.1 V	−27
		4.25–4.4 V	−20					4.2–4.4 V	−32
	4	*Charge*			*Charge*			*Charge*	
		4.0–4.2 V	−3.3		3.7–3.8 V	−4.3		3.75–3.9 V	−6.8
		4.2–4.25 V	−10.7		4.15–4.25 V	+8.4		4.0–4.1 V	−31
		4.25–4.4 V	−19.8					4.2–4.4 V	−33
	2	*Discharge*			*Discharge*			*Discharge*	
		3.5–3.0 V	+6.1		3.85–3.65 V	−8.4		4.05–4.0 V	+31
		3.8–3.65 V	+9.6		3.4–3.15 V	+6.97		3.8–3.65 V	+17
		4.2–4.0 V	+13.6					3.6–3.35 V	+16
	3	*Discharge*			*Discharge*			*Discharge*	
		3.5–3.0 V	+7		3.85–3.65 V	−5.6		4.05–4.0 V	+40
		3.8–3.65 V	+8.6		3.4–3.15 V	+7.8		3.8–3.65 V	+18
		4.2–4.0 V	+11					3.6–3.35 V	+19
	4	*Discharge*			*Discharge*			*Discharge*	
		3.5–3.0 V	+6.4		3.85–3.65 V	−5.8		4.05–4.0 V	+29
		3.8–3.65 V	+8.4		3.4–3.15 V	+8.3		3.8–3.65 V	+17
		4.2–4.0 V	+9.6					3.6–3.35 V	

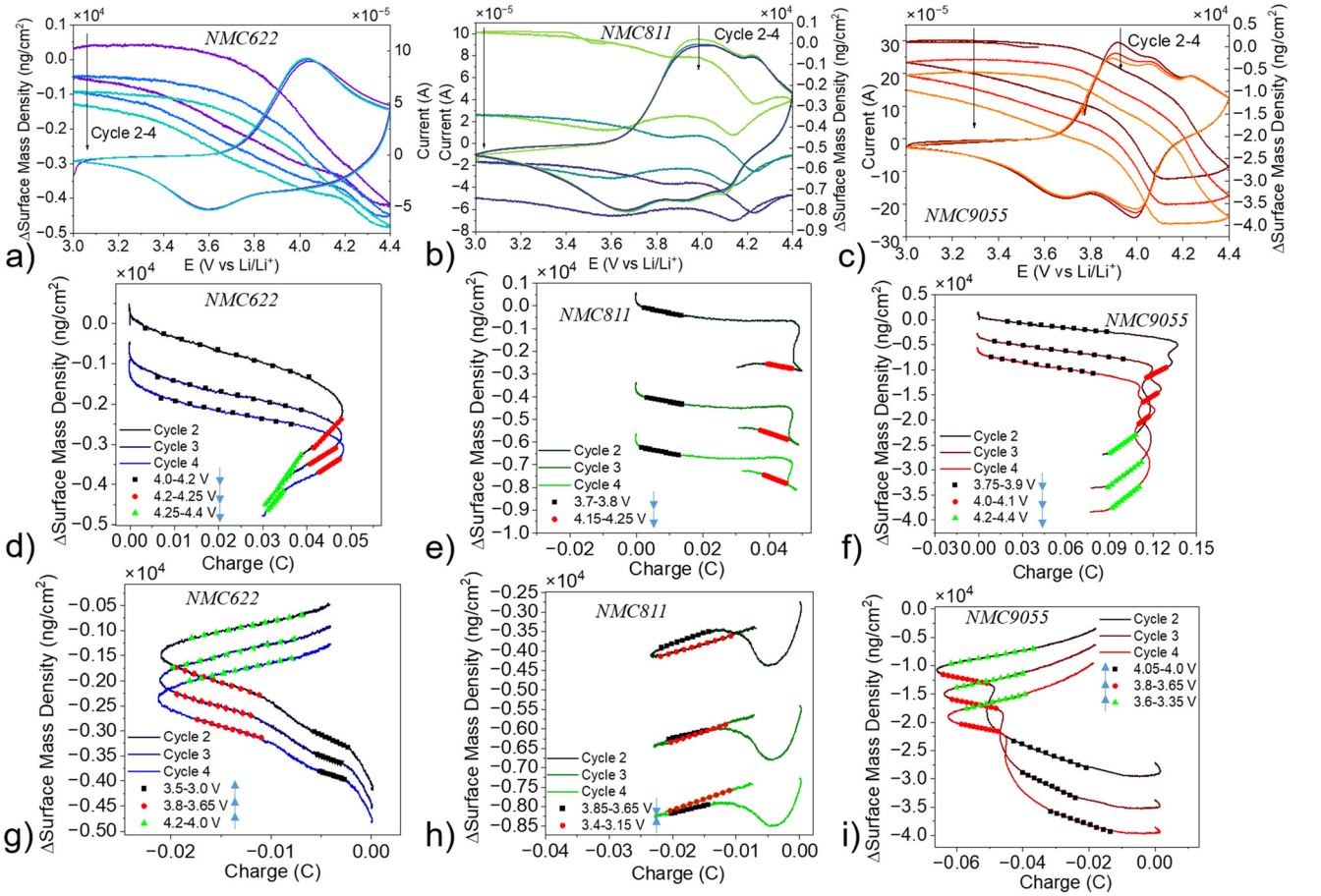

Fig. 8 CV and simultaneous surface mass density changes of (a) NMC622 (b) NMC811 and (c) NMC9055 in three-electrode EQCM cells during Cycle 2 to 4 (after initial cycle measured previously). Charge (3.0 V to 4.4 V) *versus* surface mass density change for (d) NMC622 (e) NMC811 (f) NMC9055 during oxidation of Cycle 2 to 4 (down arrows represent a mass decrease in a given potential range). Charge of reduction steps (4.4 V to 3.0 V) *versus* surface mass density change for (g) NMC622 (h) NMC811 (i) NMC9055 in three-electrode EQCM cells during Cycle 2 to 4 (up or down arrows represent a mass increase or decrease in a given potential range, respectively).

mass loss. In contrast to the oxidation step, the reduction for both NMC622 and NMC811 shows only small MPE values of <10 g mol e^-. At the same potentials where NMC622 and NMC811 showed clear signs of Li^+ insertion (3.4–3.0 V), NMC9055 shows a very high MPE, suggesting that Li^+ insertion is accompanied by deposition processes. This is consistent with the strong signal in the O 1s XPS for discharged NMC9055 electrodes. At higher potentials during the discharge process, the MPE values are similar to those measured for cycle 1, as is seen with NMC622 and NMC811.

Conclusions

In conclusion, we have explored the origin of the tradeoff between cycling potential limits for Ni-rich NMCs, NMC9055 and NMC622, and capacity/capacity retention, with particular emphasis on how the surface chemistry affects those tradeoffs. In particular, even when lower potential limits are used than for NMC622 cells, there was no cycling range in which NMC9055 and NMC622 half-cells had similar capacity retentions. Through soft XAS and XPS probing at multiple states-of-charge and -discharge for NMC9055, it was determined that its surface reaction layers can be detected at deeper probing depths compared to NMC622. XPS results largely corroborated findings from soft XAS regarding electrolyte salt decomposition, gas evolution, and consumption of surface organic compounds (for NMC622) *versus* evolution of surface organic compounds (for NMC9055) during charge. EQCM provided additional evidence of Li_2CO_3 decomposition into CO_2 and Li_2O, which were supported by XPS results. Moreover, EQCM corroborated initial electrochemical data by showing, in contrast to NMC622 and NMC811, that Li^+ insertion into NMC9055 during discharge is accompanied by deposition processes on the cathode surface. Finally, NMC9055 cathode exhibits significantly more pronounced chemical reactions that lead to dissolution or deposition of surface species during electrochemical cycling, suggesting more reactive surface nature compared to NMC622 and NMC811, despite cycling under similar capacities.

Author contributions

M. T. devised the experimental plan as well as carried out all electrochemical fabrication and characterization, all measurements and analysis of XPS samples, analysis of all soft XAS samples, and all EQCM measurements, calculations, and analysis under supervision of M. D. and W. T.; D. N. performed soft XAS measurements and provided expertise in their analysis. M. T., W. T., and M. D. wrote the original draft, and all authors reviewed and provided their edits.

Conflicts of interest

The authors have no conflicts of interest to report.

Data availability

dQ/DV and charge/discharge plots of cells containing NMC622 and NMC9055 cathodes between various voltage limits; EIS data on cells containing NMC cathodes; *ex situ* Co L-edge, O K-edge, and C K-edge XAS data on NMC cathodes at various states-of-charge; C1s, P2p Co2p, and Mn2p depth profiling XPS results on NMC cathodes at various states-of-charge; EQCM sensor with a blank film containing only carbon and PVdF; coin cell CVs of cells containing NMC cathodes. Supplementary information is available. See DOI: https://doi.org/10.1039/d6eb00021e.

Raw data presented in this work can be provided by the authors upon request.

Acknowledgements

This work was supported by the Assistant Secretary for Energy, Efficiency and Renewable Energy, Office of Vehicle Technologies of the U.S. Department of Energy under Contract No. DE-AC02-05CH11231. Work at the Molecular Foundry of Lawrence Berkeley National Lab (LBNL), supported by the Office of Science, Office of Basic Energy Sciences of the U.S. Department of Energy under Contract No. DE-AC02-05CH11231. We would like to acknowledge Dr Paul Ashby and Dr Harishankar Jayakumar for their support at the Molecular Foundry. We would like to acknowledge the use of the Stanford Synchrotron Radiation Lightsource, SLAC National Accelerator Laboratory, that is supported by the U.S. Department of Energy, Office of Science, Office of Basic Energy Sciences under Contract No. DE-AC02-76SF00515.

References

1 A. M. Andersson, D. P. Abraham, R. Haasch, S. MacLaren, J. Liu and K. Amine, *J. Electrochem. Soc.*, 2002, **149**, A1358.
2 C. Tian, F. Lin and M. M. Doeff, *Acc. Chem. Res.*, 2018, **51**, 89–96.

3 C. Tian, D. Nordlund, H. L. Xin, Y. Xu, Y. Liu, D. Sokaras, F. Lin and M. M. Doeff, *J. Electrochem. Soc.*, 2018, **165**, A696.
4 Y. Yu, P. Karayaylali, L. Giordano, J. Corchado-Garciá, J. Hwang, D. Sokaras, F. Maglia, R. Jung, F. S. Gittleson and Y. Shao-Horn, *ACS Appl. Mater. Interfaces*, 2020, **12**, 55865–55875.
5 H. Sun, Z. Yang, R. Ghosh, S. Hwang, A. Hu, Y. Zhang, J. Liu, C. Sun, S. Sainio, D. Nordlund, X. Xiao and F. Lin, *Nat. Commun.*, 2025, **16**, 1–10.
6 H. H. Ryu, B. Namkoong, J. H. Kim, I. Belharouak, C. S. Yoon and Y. K. Sun, *ACS Energy Lett.*, 2021, **6**, 2726–2734.
7 C. D. Quilty, P. J. West, W. Li, M. R. Dunkin, G. P. Wheeler, S. Ehrlich, L. Ma, C. Jaye, D. A. Fischer, E. S. Takeuchi, K. J. Takeuchi, D. C. Bock and A. C. Marschilok, *Phys. Chem. Chem. Phys.*, 2022, **24**, 11471–11485.
8 R. C. Lee, J. Franklin, C. Tian, D. Nordlund, M. Doeff and R. Kostecki, *J. Power Sources*, 2021, **498**, 229885.
9 Y. Bi, J. Tao, Y. Wu, L. Li, Y. Xu, E. Hu, B. Wu, J. Hu, C. Wang, J. G. Zhang, Y. Qi and J. Xiao, *Science*, 2020, **370**, 1313–1318.
10 J. Alvarado, C. Wei, D. Nordlund, T. Kroll, D. Sokaras, Y. Tian, Y. Liu and M. M. Doeff, *Mater. Today*, 2020, **35**, 87–98.
11 F. Lin, I. M. Markus, D. Nordlund, T. C. Weng, M. D. Asta, H. L. Xin and M. M. Doeff, *Nat. Commun.*, 2014, **5**, 1–9.
12 E. McCalla, A. M. Abakumov, M. Saubanère, D. Foix, E. J. Berg, G. Rousse, M. L. Doublet, D. Gonbeau, P. Novák, G. Van Tendeloo, R. Dominko and J. M. Tarascon, *Science*, 2015, **350**, 1516–1521.
13 S. E. Renfrew and B. D. McCloskey, *J. Electrochem. Soc.*, 2019, **166**, A2762–A2768.
14 J. Xiao, N. Adelstein, Y. Bi, W. Bian, J. Cabana, C. L. Cobb, Y. Cui, S. J. Dillon, M. M. Doeff, S. M. Islam, K. Leung, M. Li, F. Lin, J. Liu, H. Luo, A. C. Marschilok, Y. S. Meng, Y. Qi, R. Sahore, K. G. Sprenger, R. C. Tenent, M. F. Toney, W. Tong, L. F. Wan, C. Wang, S. E. Weitzner, B. Wu and Y. Xu, *Nat. Energy*, 2024, **9**, 1463–1473.
15 S.-B. Son, D. Robertson, Y. Tsai, S. Trask, A. Dunlop and I. Bloom, *J. Electrochem. Soc.*, 2020, **167**, 160508.
16 S. E. Weitzner, B. Wang, N. Rampal, W. Jeong, S. Yuan, S. Zhang, G. Bucci, N. Adelstein, S. Yan, A. C. Marschilok and L. F. Wan, *Energy Storage Mater.*, 2025, **80**, 104368.
17 S. S. Zhang, *Energy Storage Mater.*, 2020, **24**, 247–254.
18 T. Liu, L. Yu, J. Liu, J. Lu, X. Bi, A. Dai, M. Li, M. Li, Z. Hu, L. Ma, D. Luo, J. Zheng, T. Wu, Y. Ren, J. Wen, F. Pan and K. Amine, *Nat. Energy*, 2021, **6**, 277–286.
19 F. Frati, M. O. J. Y. Hunault and F. M. F. De Groot, *Chem. Rev.*, 2020, **120**, 4056–4110.
20 R. Qiao, Y. De Chuang, S. Yan and W. Yang, *PLoS One*, 2012, **7**, e49182.
21 A. S. Vinogradov, S. I. Fedoseenko, S. A. Krasnikov, A. B. Preobrajenski, V. N. Sivkov, D. V. Vyalikh, S. L. Molodtsov, V. K. Adamchuk, C. Laubschat and G. Kaindl, *Phys. Rev. B: Condens. Matter Mater. Phys.*, 2005, **71**, 045127.
22 J. Wang, Y. Shin, E. Arenholz, B. M. Lefler, J. M. Rondinelli and S. J. May, *Phys. Rev. Mater.*, 2018, **2**, 073407.
23 I. Hasa, A. M. Haregewoin, L. Zhang, W. Y. Tsai, J. Guo, G. M. Veith, P. N. Ross and R. Kostecki, *ACS Appl. Mater. Interfaces*, 2020, **12**, 40879–40890.
24 R. Qiao, I. T. Lucas, A. Karim, J. Syzdek, X. Liu, W. Chen, K. Persson, R. Kostecki and W. Yang, *Adv. Mater. Interfaces*, 2014, **1**, 1300115.
25 K. Medjanik, A. Chernenkaya, X. Kozina, S. A. Nepijko, G. Öhrwall, P. Foury-Leylekian, P. Alemany, G. Schönhense, E. Canadell and J. P. Pouget, *J. Phys. Chem. A*, 2016, **120**, 8574–8583.
26 S. Sainio, N. Wester, A. Aarva, C. J. Titus, D. Nordlund, E. I. Kauppinen, E. Leppänen, T. Palomäki, J. E. Koehne, O. Pitkänen, K. Kordas, M. Kim, H. Lipsanen, M. Mozetič, M. A. Caro, M. Meyyappan, J. Koskinen and T. Laurila, *J. Phys. Chem. C*, 2021, **125**, 973–988.
27 B. J. Schultz, C. Jaye, P. S. Lysaght, D. A. Fischer, D. Prendergast and S. Banerjee, *Chem. Sci.*, 2012, **4**, 494–502.
28 F. Huttmann, D. Klar, N. Atodiresei, C. Schmitz-Antoniak, A. Smekhova, A. J. Martínez-Galera, V. Caciuc, G. Bihlmayer, S. Blügel, T. Michely and H. Wende, *Phys. Rev. B*, 2017, **95**, 075427.
29 M. Sathiya, G. Rousse, K. Ramesha, C. P. Laisa, H. Vezin, M. T. Sougrati, M. L. Doublet, D. Foix, D. Gonbeau, W. Walker, A. S. Prakash, M. Ben Hassine, L. Dupont and J. M. Tarascon, *Nat. Mater.*, 2013, **12**, 827–835.
30 N. Yabuuchi, K. Yoshii, S. T. Myung, I. Nakai and S. Komaba, *J. Am. Chem. Soc.*, 2011, **133**, 4404–4419.
31 T. G. Avval, S. Chatterjee, S. Bahr, P. Dietrich, M. Meyer, A. Thißen and M. R. Linford, *Surf. Sci. Spectra*, 2019, **26**, 014022.
32 P. S. Bagus, E. S. Ilton and C. J. Nelin, *Surf. Sci. Rep.*, 2013, **68**, 273–304.
33 A. I. Stadnichenko, S. V. Koshcheev and A. I. Boronin, *Moscow Univ. Chem. Bull.*, 2007, **62**, 343–349.
34 J. Onoe, K. Takeuchi, K. Ohno and Y. Kawazoe, *J. Vac. Sci. Technol., A*, 1998, **16**, 385–388.
35 K. R. Tallman, G. P. Wheeler, C. J. Kern, E. Stavitski, X. Tong, K. J. Takeuchi, A. C. Marschilok, D. C. Bock and E. S. Takeuchi, *J. Phys. Chem. C*, 2021, **125**, 58–73.
36 O. Bondarchuk, A. P. LaGrow, A. Kvasha, T. Thieu, E. Ayerbe and I. Urdampilleta, *Appl. Surf. Sci.*, 2021, **535**, 147699.
37 Nickel (Ni), Z = 28, & Nickel Compounds, https://xpsdatabase.net/nickel-ni-z28-chemicals, (accessed 18 June 2025).
38 Cobalt (Co), Z = 27, https://xpsdatabase.net/cobalt-co-z27, (accessed 18 June 2025).
39 Manganese (Mn), Z = 25, & Manganese Compounds, https://xpsdatabase.net/manganese-mn-z25-chemicals, (accessed 18 June 2025).
40 J. Cazaux, *J. Electron Spectrosc. Relat. Phenom.*, 1999, **105**, 155–185.
41 J. Cazaux, *J. Electron Spectrosc. Relat. Phenom.*, 2000, **113**, 15–33.
42 N. Shpigel, M. D. Levi, S. Sigalov, O. Girshevitz, D. Aurbach, L. Daikhin, P. Pikma, M. Marandi, A. Jänes,

E. Lust, N. Jäckel and V. Presser, *Nat. Mater.*, 2016, **15**, 570–575.

43 N. Shpigel, S. Sigalov, M. D. Levi, T. Mathis, L. Daikhin, A. Janes, E. Lust, Y. Gogotsi and D. Aurbach, *Joule*, 2018, **2**, 988–1003.

44 N. Shpigel, M. R. Lukatskaya, S. Sigalov, C. E. Ren, P. Nayak, M. D. Levi, L. Daikhin, D. Aurbach and Y. Gogotsi, *ACS Energy Lett.*, 2017, **2**, 1407–1415.

45 X. Song, T. Liu, J. Amine, Y. Duan, J. Zheng, Y. Lin and F. Pan, *Nano Energy*, 2017, **37**, 90–97.

46 P. Jiménez, E. Levillain, O. Alévêque, D. Guyomard, B. Lestriez and J. Gaubicher, *Angew. Chem., Int. Ed.*, 2017, **56**, 1553–1556.

47 V. Dargel, N. Shpigel, S. Sigalov, P. Nayak, M. D. Levi, L. Daikhin and D. Aurbach, *Nat. Commun.*, 2017, **8**, 1–8.

48 J. T. Li, S. R. Chen, X. Y. Fan, L. Huang and S. G. Sun, *Langmuir*, 2007, **23**, 13174–13180.

49 D. Bartow, E. Peled, L. Burstein, Y. Ozawa, R. Yazami and B. Fultz, *J. Electrochem. Soc.*, 1998, **145**, 2629.

50 Z. W. Yin, X. X. Peng, J. T. Li, C. H. Shen, Y. P. Deng, Z. G. Wu, T. Zhang, Q. B. Zhang, Y. X. Mo, K. Wang, L. Huang, H. Zheng and S. G. Sun, *ACS Appl. Mater. Interfaces*, 2019, **11**, 16214–16222.

51 Z. Yang, M. C. Dixon, R. A. Erck and L. Trahey, *ACS Appl. Mater. Interfaces*, 2015, **7**, 26585–26594.